Electronic Supplementary Information

Nickel Phosphide Polymorphs with Active (001) Surface as Excellent Catalysts for Water Splitting

Chan Su Jung,[a] Kidong Park,[a] Yeron Lee,[a] In Hye Kwak,[a] Ik Seon Kwon,[a]
Jundong Kim,[a] Jaemin Seo,[a] Jae-Pyoung Ahn,[b] and Jeunghee Park,[a]*

[a] Department of Chemistry, Korea University, Jochiwon 339-700, Republic of Korea.

[b] Korea Advanced Analysis Center, Korea Institute of Science and Technology, Seoul 136-791, Republic of Korea.

Contents

Fig. S10 NBED pattern and strain maps of Ni_2P NW.

Fig. S11 NBED pattern and strain maps of Ni_5P_4 NW.

Fig. S12 SEM, XRD, and XPS data before and after the OER.

Fig. S13 *In situ* Raman spectra of Ni_2P NWs during OER.

Fig. S14 and **Table S3**. H_2 and O_2 evolution for Ni_2P NWs under an applied potential of -0.1 V (vs. RHE) in pH 13.

IV. References

I. Experimental

Structural Characterization. The structures and compositions of the products were analyzed by scanning electron microscopy (SEM, Hitachi S-4700), field-emission transmission electron microscopy (TEM, FEI TECNAI G^2 200 kV), high-voltage TEM (HVEM, Jeol JEM ARM 1300S, 1.25 MV), and energy-dispersive X-ray fluorescence spectroscopy (EDX). For the identification of composition, scanning transmission electron microscopy (STEM) and energy-dispersive X-ray fluorescence spectroscopy (EDX) with elemental maps were acquired using TEM (FEI Talos F200X) operated at 200 keV that equipped with high-brightness Schottky field emission electron source (X-FEG) and Super-X EDS detector system (Bruker Super-X). This EDX has powerful sensitivity and resolution in the low photon energy region.

High-resolution X-ray diffraction (XRD) patterns were obtained using the 9B and 3D beam lines of the Pohang Light Source (PLS) with monochromatic radiation. X-ray photoelectron spectroscopy (XPS) measurements were performed using the 8A1 beam line of the PLS, as well as a laboratory-based spectrometer (Thermo Scientific Theta Probe) using a photon energy of 1486.6 eV (Al Kα). X-ray absorption spectroscopy (XAS) measurements were carried out at the PLS elliptically polarized undulator beamline, 2A.

For the TEM analysis of the cross section, we prepared the sample as follows; (1) as-grown Ni_2P NWs or Ni_5P_4 NSs were detached from the substrates and dispersed in isopropanol (IPA) using sonication, (2) transferred to a silicon substrate by dropping the IPA solution, (3) 80 nm-thick C layers were deposited using a general C coater, (4) 30 nm-thick Pt layers were deposited onto the C layers using electron beam, (5) 2.5 μm-thick Pt layers were deposited using focused ion (gallium) beam (FIB), (6) the slice was fabricated by milling the Pt- Ni_2P (or Ni_5P_4)-Si substrate using FIB.

The strain mappings were acquired using TEM (FEI TECNAI G^2 200 kV) operated at 200 keV. Both scanning and precession were enabled through a NanoMEGAS Digistar system hardwired into the microscope scan control boards. The system was controlled through the NanoMEGAS TOPSIN software package using a Stingray fast capture CCD camera to capture the diffraction patterns as seen on the small viewing screen of the microscope. The precession diffraction measurements based on the principle of nanobeam electron diffraction (NBED), and the STEM coils are used to process the electron beam. As a consequence of NBED, a script written in Digital Micrograph is required to scan the beam across the specimens and individually save the acquired patterns. This has been done using software TOPSPIN so that large deformation maps can be acquired using many thousands of diffraction patterns. For the measurement of deformation in the NW, an array of 100 × 50 diffraction patterns was acquired using a step size of only 1.75 nm. A precession angle of 0.25° was used to provide a probe of less than 2 nm in diameter.

In-situ Raman spectra were measured with a homemade micro-Raman system with electrochemical cells. The spectral resolution is about 1 cm^{-1}. Raman scattering signals were obtained in a back-scattering configuration using a 100× objective (NA 0.9) and an Ar ion laser with a wavelength of 514.5 nm. The laser spot size was approximately 1 μm, which, in combination with the imaging capabilities of the microscope. A laser power below 0.5 mW was used to avoid heating effects.

Electrochemical measurements. Electrochemical experiments were carried out at room temperature in a three-electrode cell connected to an electrochemical analyzer

(CompactStat, Ivium Technologies). A saturated calomel electrode (SCE, KCl saturated, Basi Model RE-2BP) or Ag/AgCl electrode (saturated with 4M KCl, Pine Co) was used as the reference electrode, respectively, at pH 0 (0.5 M H_2SO_4) and pH 14 (1 M KOH). A graphite rod (6 mm dia. × 102 mm long, 99.9995%, Alfa Aesar) or coiled Pt coil (0.5 mm dia., Pine Instrument) was used as the counter electrode. As-grown samples on Ni foil or foam was used directly as the working electrode. The edge of the sample was sealed with epoxy resin, and the exposed area was 1 cm^2. A piece of Cu wire was used to connect the sample with the external circuit through a metal (Au) alligator clip. The Pt/C (20 wt.% Pt in Vulcan, Aldrich-Sigma) or IrO_2 electrodes were prepared by drop-casting the samples (0.2 mg dispersed in Nafion using isopropyl alcohol) over a glassy carbon electrode (area = 0.1963 cm^2, Pine Instruments Model No. AFE5T050GC). A rotation speed of 1600 rpm was used for the linear sweep voltammetry (LSV) measurements. IrO_2 powders were purchased from Aldrich. The average size of IrO_2 is 10 nm.

For HER, the potential measured against the reference electrode, E (V vs. Ag/AgCl) or E (V vs. SCE), was converted to the potential against the reversible hydrogen electrode (RHE) using the following equations

$$E\ (\text{V vs. RHE}) = E\ (\text{V vs. Ag/AgCl}) + E_{\text{Ag/AgCl}}\ (= 0.197\ \text{V}) + 0.0592\ \text{pH}\ (\text{V})\ \text{or}$$

$$E\ (\text{V vs. RHE}) = E\ (\text{V vs. SCE}) + E_{\text{SCE}}\ (= 0.241\ \text{V}) + 0.0592\ \text{pH}\ (\text{V}).$$

Therefore, in a 0.5 M H_2SO_4 (pH = 0) electrolyte, E (vs. RHE) = E (vs. SCE) + 0.241 V, and in a 1 M KOH (pH = 14) electrolyte, E (vs. RHE) = E (vs. Ag/AgCl) + 0.197 V + 0.8288 V = E (vs. Ag/AgCl) + 1.0258 V. All the polarization curves in this work were corrected by eliminating iR drop with respect to the ohmic resistance of the solution using a CompactStat Software. The electrolyte was purged with ultrahigh purity H_2 gas during the measurement to ensure electrolyte saturation. Electrocatalysis was measured using linear sweeping from +0.2 to −1.0 V (vs. RHE) with a scan rate of 1-10 mV s^{-1}.

The hydrogen (H_2) and oxygen (O_2) gas evolution by the PEC water splitting was conducted in the airtight reactor, and was monitored using gas chromatography (GC, Young Lin ACME 6100). A pulsed discharge detector (VICI, Valco Instruments Co., Inc.) and a GC column (SUPELCO Molecular Sieve 13X) with a length of 3 ft. and an inner diameter of 1/8 in were used. The quantities of H_2 and O_2 were calibrated using a standard H_2/He and O_2/He mixture.

For OER, a Ag/AgCl electrode and a Pt wire were used as reference and counter electrodes, respectively. Before the electrochemical measurement, the electrolyte (0.1 M or 1 M KOH) was purged by O_2 (ultrahigh grade purity) for at least 0.5 h to ensure electrolyte saturation. The potentials reported in our work were referenced to the RHE through standard RHE calibration of applied potential: E (vs. RHE) = E (vs. Ag/AgCl) + $E_{Ag/AgCl}$ (= 0.197 V) + 0.0592 pH = E (vs. Ag/AgCl) + 1.0258 V in 1 M KOH and E (vs. RHE) = E (vs. Ag/AgCl) + 0.9666 V in 0.1 M KOH. The overpotential (η) is defined as E (vs. RHE) − 1.229 V.

Electrochemical impedance spectroscopy (EIS) measurements were carried out for the electrode in an electrolyte by applying an AC voltage of 10 mV in the frequency range of 100 kHz to 0.1 Hz at a bias voltage of -0.15 V (vs. RHE). To measure double-layer capacitance via cyclovoltammetry (CV), a potential range in which no apparent Faradaic processes occur was determined from static CV. All measured current in this non-Faradaic potential region is assumed to be due to double-layer capacitance. The charging current, i_c, is then measured from CVs at multiple scan rates. The working electrode was held at each potential vertex for 10 s before beginning the next sweep. The double-layer capacitance current density (J) is equal to the product of the scan rate (ν) and the electrochemical double-layer capacitance (C_{dl}), as given by equation $J = \nu\ C_{\mathrm{dl}}$, Thus, a plot of J as a function of ν yields a straight line with a slope equal to C_{dl}. The scan rates were 20–100 mV s^{-1}.

Density of electrochemically active site and turnover frequency. The electrochemically active site density and per-site turnover frequency (TOF) have been estimated as follows. It should be emphasized that since the nature of the active sites of the catalyst is not clearly understood yet and the real surface area for the nanostructured heterogeneous catalyst is hard to accurately determine, the following result is really just an estimation.

To estimate the active surface site density, we used the C_{dl} value (see Fig. S9, 16.3 and 16.7 mF cm^{-2} (before 500th cycles) , respectively, for Ni_2P and Ni_5P_4, and calculated the electrochemically active surface area (ECSA), which is equivalent to the roughness factor; C_{dl}/C_s, where C_s is the specific surface capacitance of the electrode surface. Since the exact value of C_s for Ni_2P or Ni_5P_4 is not available, a commonly used C_s value (0.035 mF cm^{-2} in acid and 0.040 mF cm^{-2} in base) for metal surfaces was used.[S1] Then the roughness factor (basically the surface area ratio between the catalyst vs. the metal electrodes), is 16.3 mF cm^{-2}/0.035 mF cm^{-2} = 466 for Ni_2P and 16.7 mF cm^{-2}/0.035 mF cm^{-2} = 477 for Ni_5P_4.

The density of surface sites was reported as 2.0001×10^{15} and 1.8889×10^{15} site cm^{-2}, respectively.[S2,S3] The density of surface active sites (m) of Ni_2P and Ni_5P_4 on geometric area: 2.001×10^{14} atom $cm^{-2} \times 466$ (= roughness factor) = 9.32×10^{16} atom cm^{-2} and 1.8889×10^{14} atom $cm^{-2} \times 477$ (= roughness factor) = 9.01×10^{16} atom cm^{-2}

The total number of hydrogen (H_2) gas turns overs was calculated from the current density (J in mA cm^{-2}) according to n_{H2} = J (mA cm^{-2})/1000 mA × 1 C s^{-1} × 1 mol e^{-}/96486

C × (1 mol H_2/2 mol e^{-1}) × (6.022×10^{23} H_2 molecules/1 mol H_2) = 3.12×10^{15} H_2 s^{-1} cm^{-2} per mA cm^{-2}.

For Ni_2P, the per-site TOF at $\eta = 0.15$ V (with a current density of 18 mA cm^{-2} at pH 0) is n_{H2}/m (= density of surface active sites) = $18 \times 3.12 \times 10^{15}$ H_2 s^{-1} cm^{-2} / 9.32×10^{16} atom cm^{-2} = 0.58 H_2 s^{-1}. In the case of Ni_5P_4 with a current density of 34 mA cm^{-2} at pH 0), the TOF was estimated as 1.2 s^{-1}, respectively, at 0.15 V.

We summarized the TOF values at 0.15 V as follows.

Guest	J (mA cm^{-2}) at 0.15 V	n_{H2}	Roughness factor	m	TOF (s^{-1})
Ni_2P	17.4	5.43×10^{16}	466	9.32×10^{16}	0.58
Ni_5P_4	34.0	1.06×10^{17}	477	9.01×10^{16}	1.18
Ni_5P_4 (after 500 cycles)	13.2	4.12×10^{16}	195	3.68×10^{16}	1.12

II. Supporting Tables

Table S1. HER electrocatalytic efficiency of Ni_2P and Ni_5P_4 nanostructures synthesized by phosphorization of Ni substrates reported in the previous works.

No.	Sample	Loading	Electrolyte	*J* (mAcm^{-2})	η$_{J=10}$ (mV)[a]	Tafel slope (mV dec^{-1})	Reference [b]
1	**Ni_2P**	3.5 mg cm^{-2} nanosheets on Ni foam	0.5 M H_2SO_4 1.0 M PBS 1 M KOH	15 5 10	175 175 175	68 142 50	S4 [18]
2	**Ni_2P**	Nanorods on Ni foam	0.5 M H_2SO_4	10	131	106	S5 [21]
3	**Ni_5P_4-Ni_2P**	68.2 mgcm^{-2} nanosheets on Ni foam	0.5 M H_2SO_4	10	120	79.1	S6 [22]
4	**Ni_5P_4**	13.9 mg Nanosheets on Ni foil (2 cm × 2cm) (=3.5 mg cm^{-2})	0.5 M H_2SO_4 1 M KOH	10 10	140 150	40 53	S7 [23]
5	**Ni_2P**	3.5 mg cm^{-2} nanowires on Ni foil or foam	0.5 M H_2SO_4 1 M KOH	10	123 240	42 80	Our work
	Ni_5P_4	45 mg cm^{-2} Nanosheets	0.5 M H_2SO_4 1 M KOH		114 190	34 70	

[a] Overpotential (η) that delivers a current density (*J*).

[b] The number in the parenthesis is its corresponding numbers in the text.

Table S2. OER electrocatalytic efficiency of various nickel phosphide polymorphs, reported in the previous works.

	Loading[a]	**Electrolyte**	**J (mA cm^{-2})**[b]	**η (mV)**[b]	**Tafel slope (mV dec^{-1})**	**Reference**[c]
Ni_5P_4	13.9 mg Nanosheets on Ni foil (=3.5 mg cm^{-2})	1 M KOH	10	330	40	S7 [23]
Ni_2P	0.14 mg cm^{-2} on GC	1 M KOH	10	290	47	S8 [38]
Ni_2P	0.1 mg cm^{-2} on GC	1M KOH	10	400	60	S9 [39]
Ni_2P/Ni	Ni_2P/Ni on NF	1 M KOH	10	200	-	S10 [26]
$Ni@Ni_9P_8$	$Ni@Ni_9P_8$ on NF	1M KOH	10	-	73.2	S11 [27]
Ni_5P_4	0.15 mg cm^{-2} NPs and NWs on GC	1 M KOH	10	340	72.2	S12 [28]
Ni_2P- Ni_5P_4	0.2 mg cm^{-2} on GC	1 M KOH	10	300	64	S13 [40]
Ni_2P- Ni_5P_4	Ni_2P- Ni_5P_4 on NF	1 M KOH	10	220	23.0	S14 [41]
$Ni_{12}P_5$	1 mg cm^{-2} on FTO	1 M KOH	10	295	106	S15 [30]
$(Ni_{0.33}Fe_{0.67})_2P$	$(Ni_{0.33}Fe_{0.67})_2P$ on NF	1 M KOH	50	214	55.9	S16 [31]
Mg-Ni_2P	Mg-modified Ni_2P on CF	1 M KOH	10	290	48	S17 [42]
$N_{1-x}Co_xP$	3.5 mg cm^{-2} on GC	1 M KOH	10	266	81	S18
Ni_2P	Ni_2P on Ni foil	1 M KOH	10	350	65	Our work

[a] NPs = nanoparticles, NWs = nanowires, GC = Glassy carbon, NF = nickel foam, CF= Carbon paper; [b] Overpotential (η) that delivers a current density (*J*); [c] [b] the number in the parenthesis is its corresponding numbers in the text.

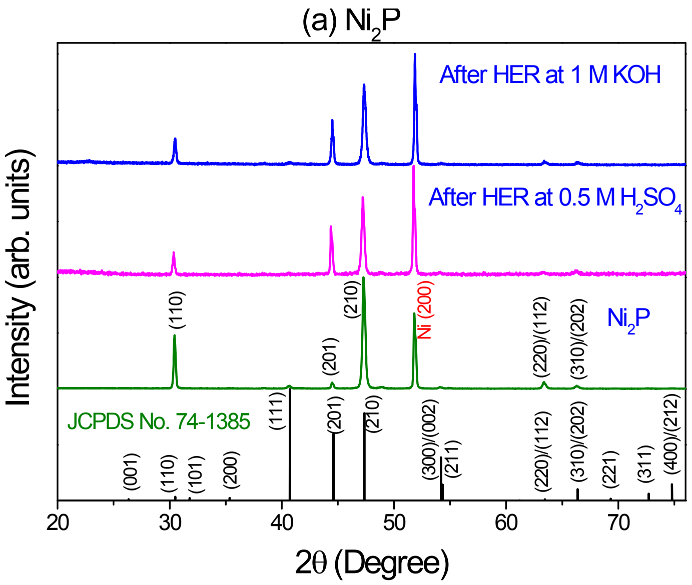

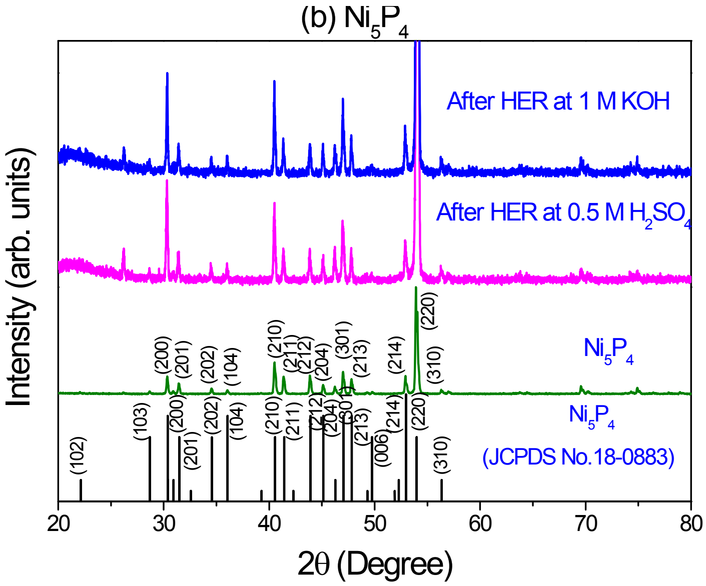

Fig. S1 XRD pattern of (a) Ni_2P and (b) Ni_5P_4, before and after 500th LSV scan (24 h) in 0.5 M H_2SO_4 (pH 0) and 1 M KOH (pH 14) electrolytes. The reference peaks of the hexagonal phase Ni_2P (JCPDS No. 74-1385, P62m, a = 5.859 Å, c = 3.382 Å), and Ni_5P_4 (JCPDS No. 18-0883, P63mc, a = 6.789 Å, c = 10.986 Å), are plotted. The peaks of the samples are well matched to those of Ni_2P and Ni_5P_4. Because the probe depth of the XRD is longer than 1 μm, the Ni (200) peak originates from the Ni foil underneath the Ni_2P. The Ni_5P_4 samples exhibit no Ni peak, indicating at least 1 μm-thick Ni foil underneath transformed into the Ni_5P_4 phase. The XRD confirm that the phase is unchanged after the HER.

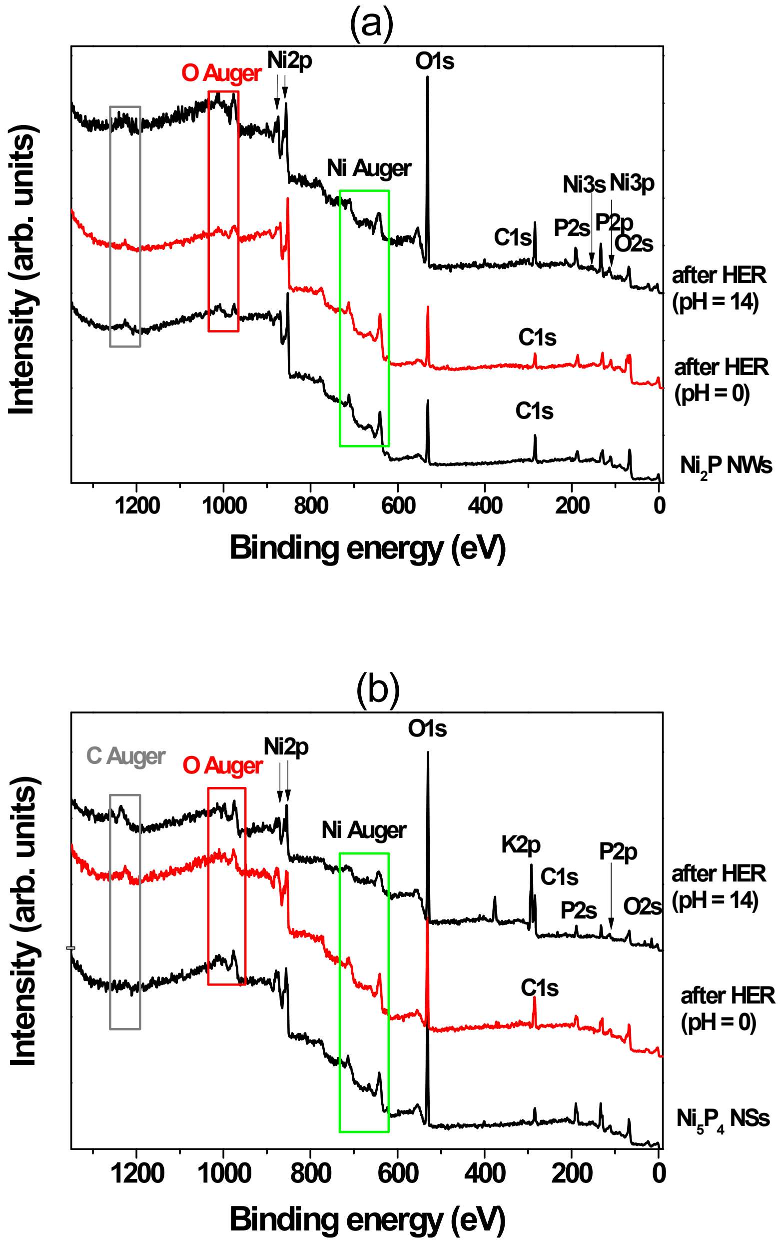

Fig. S2 Survey-scanned XPS spectrum of (a) Ni_2P NWs and (b) Ni_5P_4 NSs, before and after the 500th LSV cycle (24 h) in 0.5 M H_2SO_4 (pH 0) and 1 M KOH (pH 14) electrolytes. All spectra show the Ni and P peaks. The Ni_2P shows the relatively lower intensity of O peak than the Ni_5P_4. After HER at pH 14, the K 2p peak appears because of KOH electrolyte. The intensity of O peaks increases significantly.

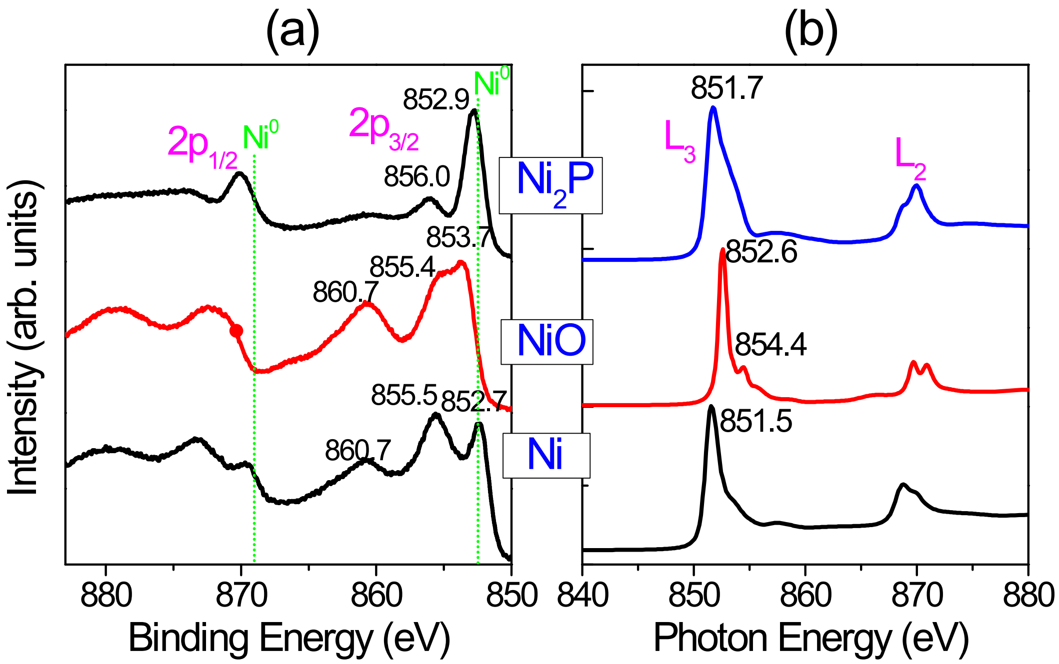

Fig. S3 (a) Fine-scanned Ni $2p_{3/2}$ and $2p_{1/2}$ peaks of Ni foil (Sigma-Aldrich, 99.99 %), NiO powders (Sigma-Aldrich, 98 %), and Ni_2P NWs. The position of the neural element peak is marked by a dotted line to delineate the shift. (b) XAS spectra of the Ni $L_{2,3}$ edge, measured at room temperature, for Ni foils, NiO powders, and Ni_2P NWs. The spectra that results from the $2p \rightarrow 3d$ dipole transition are divided into L_3 ($2p_{3/2}$) and L_2 ($2p_{1/2}$) regions.

(a) The Ni foil shows a $2p_{3/2}$ peak at 852.7 eV, corresponding to neutral Ni (Ni^0), and another one at 855.5 eV, corresponding to surface oxide form. The $2p_{3/2}$ peak of NiO consisted of two bands at 853.7 and 855.4 eV. They were blue shifted by 1.0 and 2.7 eV from the peak position of neutral Ni (Ni^0) at 852.7 eV. The first and second bands were assigned to the Ni-O bonding structures of Ni^{2+} and Ni^{3+} ions, respectively. For both samples, there was a shake-up satellite peak at 860.7 eV. For Ni_2P NWs, the peak at 852.9 eV is blue shifted by 0.2 eV relative to Ni^0, suggesting that the Ni ions have the lower oxidation number than +2, for example Ni^+. The peak at 856.0 eV is assigned to the Ni^{3+} states.

(b) It is noted that XAS can give more averaged information on the electronic structures underneath the surface due to the longer probing depth than that of XPS, which is about

10 nm.[S19,S20] The XAS L_3 peak of the Ni foil at 851.5 eV is assigned to neutral Ni^0 (Ni-Ni bonds). Two peaks of NiO powders at 852.6 and 854.4 eV are assigned to the Ni^{2+} and Ni^{3+} states, respectively. In the case of Ni_2P NWs, the peak appears at 851.7 eV, indicating that the electronic structure of Ni ions is closer to that of Ni metals.

(a) Ni_2P

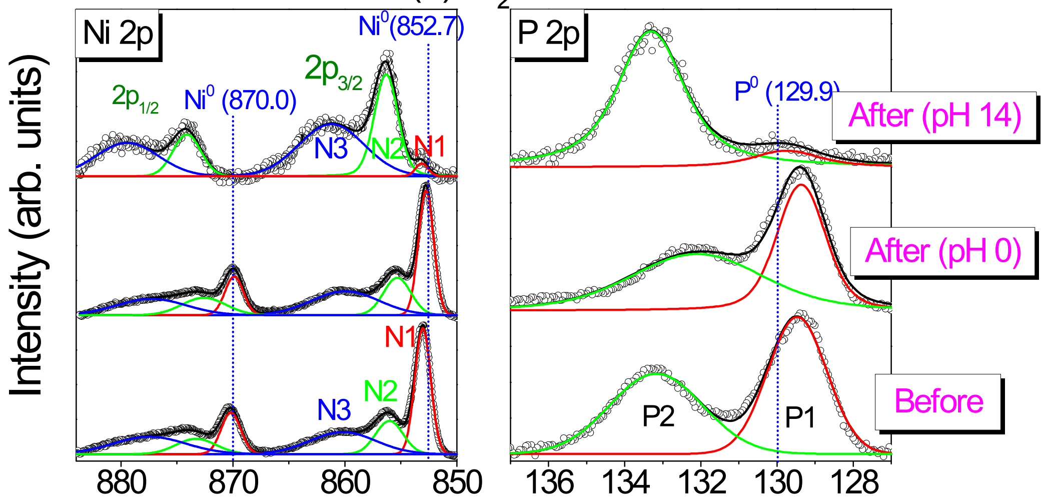

(b) Ni_5P_4

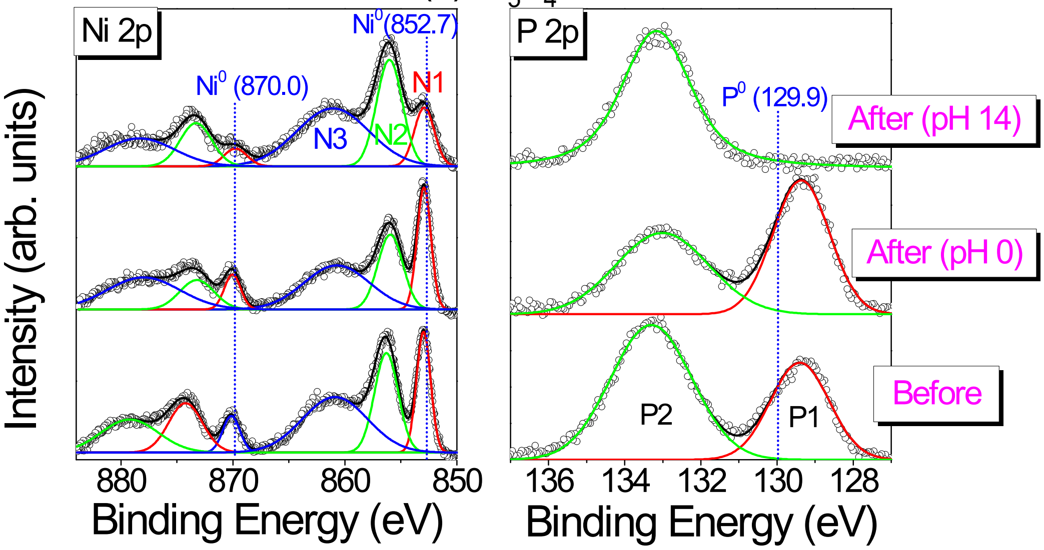

Fig. S4 Fine-scan Ni $2p_{3/2}$ and $2p_{1/2}$ peaks, and P 2*p* peaks of (a) Ni_2P and (b) Ni_5P_4, before and after the 500th cycles (24 h) in 0.5 M H_2SO_4 (pH 0) and 1 M KOH (pH 14) electrolytes. The XPS data (open circles) are fitted by a Voigt function, and the sum of the resolved bands is represented by a black line. The position of the neural element peak is marked by a dotted line to delineate the shift.

Because the probe depth is a few nanometers for the photoelectrons of Ni 2*p* and P 2*p*, the XPS peaks of the sample come solely from the Ni_2P NWs and the Ni_5P_4 NSs, which are not from the substrates.[S21,S22] The peak feature is consistent with the freestanding Ni_2P and $Ni_{12}P_5$ nanoparticles,[S23,S24] and the Ni_2P nanosheets on Ni foam.[S25]

For as-grown samples (before scan), the *2p*$_{3/2}$ peak consisted of three bands N1-N3 at 852.9 (0.2), 856.0 (3.3), and 861-862 eV, respectively. The value in parenthesis represents the blue shift from the peak position of neutral Ni^0 (852.7 eV). The N1 band mainly originates from the Ni-P bonding structures with the lower oxidation states than Ni^{2+} such as Ni^+. The N2 band is assigned to the Ni^{3+} states of Ni-P and/or that of Ni-O on surface. The N3 band corresponds to the shake-up satellite peak that originated from the population of high oxidation states. This assignment is supported by the XPS measured for the reference samples: Ni foil and NiO powders, as shown in Figure S3. The ratio of N2/N1 bands is about 0.4 and 1.1 for Ni_2P and Ni_5P_4, respectively, rationalizing the higher oxidation number of Ni in Ni_5P_4 than that in Ni_2P. It indicates that the Ni_2P is more metallic than the Ni_5P_4.

After the 500th LSV cycles in 0.5 M H_2SO_4, the XPS spectrum remain nearly the same as that of the as-grown samples. The intensity ratio of N2/N1 bands decreases, suggesting the reduction of surface oxide form. In 1 M KOH, the intensity ratio increases probably due to the surface oxidation. The XRD pattern confirmed that the phase is unchanged.

The Ni_2P and Ni_5P_4 show the P $2p_{3/2}$ peak at 129.4 eV, which is red shifted by 0.5 eV from the neutral P (P^0) peak (129.9 eV for $2p_{3/2}$). This P1 band at 129.4 V originates from the negatively charged P ion of the P-Ni bonding structures. The blue shifted band (P2) at 133.2 eV is ascribed to the P-O bond of the oxide form. The ratio of P2/P1 bands is about 0.5 and 1.3 for Ni_2P and Ni_5P_4. The Ni_2P has a less oxide form, probably due to the lower oxidation number of Ni than that in Ni_5P_4. It also supports that the Ni_2P is more metallic than the Ni_5P_4. After the 500 cycles in 0.5 M H_2SO_4, the intensity of P-O band decreases with a red shift. The spectra after the 500 cycles in 1 M KOH shows the relatively stronger P2 band than the P1 band, which is plausibly due to the surface oxide layers whose thickness is larger than 1 nm.

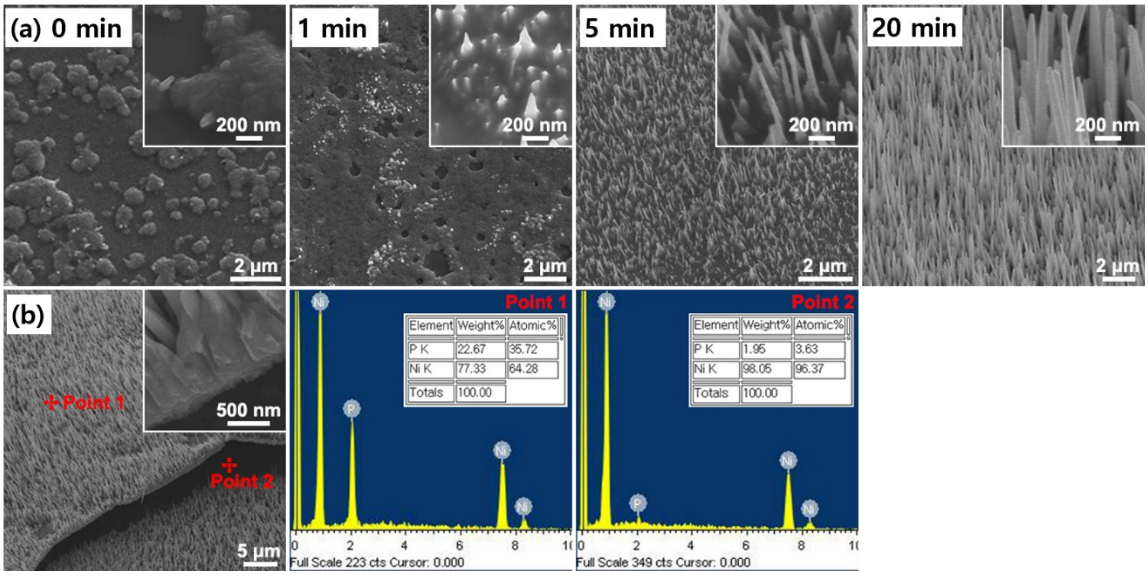

Point 1

Element	Weight%	Atomic%
P K	22.67	35.72
Ni K	77.33	64.28
Totals	100.00	

Point 2

Element	Weight%	Atomic%
P K	1.95	3.63
Ni K	98.05	96.37
Totals	100.00	

Fig. S5 (a) SEM images for the Ni foil after 0, 1, 5, and 20 min of growth time, revealing the growth process of Ni_2P NWs at 200 °C. (b) SEM images and EDX data for fully-grown Ni_2P NWs after 20 min, showing Ni:P = 2:1 for the NWs (point 1) and Ni substrates (point 2).

(a) PH_3 is preheated at 400 °C and the Ni foils are placed at 200 °C. The nanosize grains are initially formed on the Ni foils, the NWs are popped from the grains, and grown progressively with time. (b) The EDX data indicates that the Ni remains underneath the Ni_2P NWs.

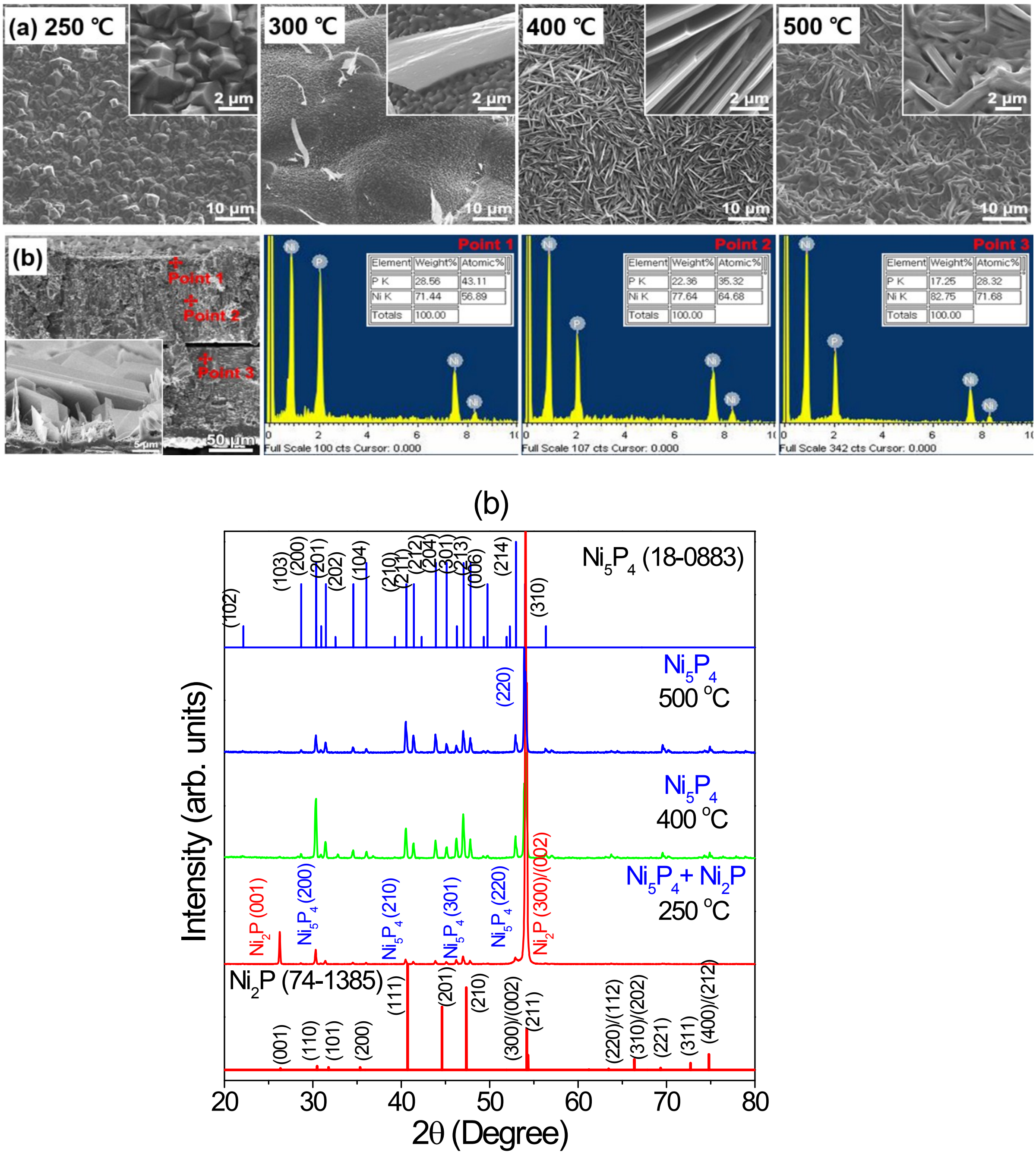

Fig. S6 (a) SEM images and (c) XRD patterns for the nanostructures grown on the Ni foils at 250, 300, 400, and 500 °C, for 2 h growth time. (b) Side-view SEM images for fully-grown Ni_5P_4 NSs and EDX data, showing Ni:P = 5:4 for the NSs (point 1), Ni:P = 2:1 for the underneath film (point 2), and Ni:P= 7:3 for the substrates (point 3). The reference peaks of hexagonal phase Ni_2P (JCPDS No. 74-1385, P2m, *a* = 5.859 Å, *c* = 3.382 Å) and hexagonal phase Ni_5P_4 (JCPDS No. 18-0883, 63mc, *a* = 6.789 Å, *c* = 10.986

Å) are plotted. The 250 °C sample shows both the Ni_2P and Ni_5P_4 phases. The 400 °C and 500 °C samples (nanosheets) shows only the Ni_5P_4 phase, whose peak position is well matched to that of the reference.

The Ni foils are placed at the heating zone in a CVD reactor. The Ni_5P_4 NSs are grown at 400-450 °C. The morphology of samples at 250 and 300 °C suggests that the nanosize grains of Ni_2P are initially formed on the Ni foils, and the Ni_5P_4 NSs are grown at cracks between the Ni_2P grains. The Ni_2P layers (400-500 nm thickness, point 2) exists underneath the Ni_5P_4 NSs (point 1), and the Ni substrates (point 3) underneath the Ni_2P layers.

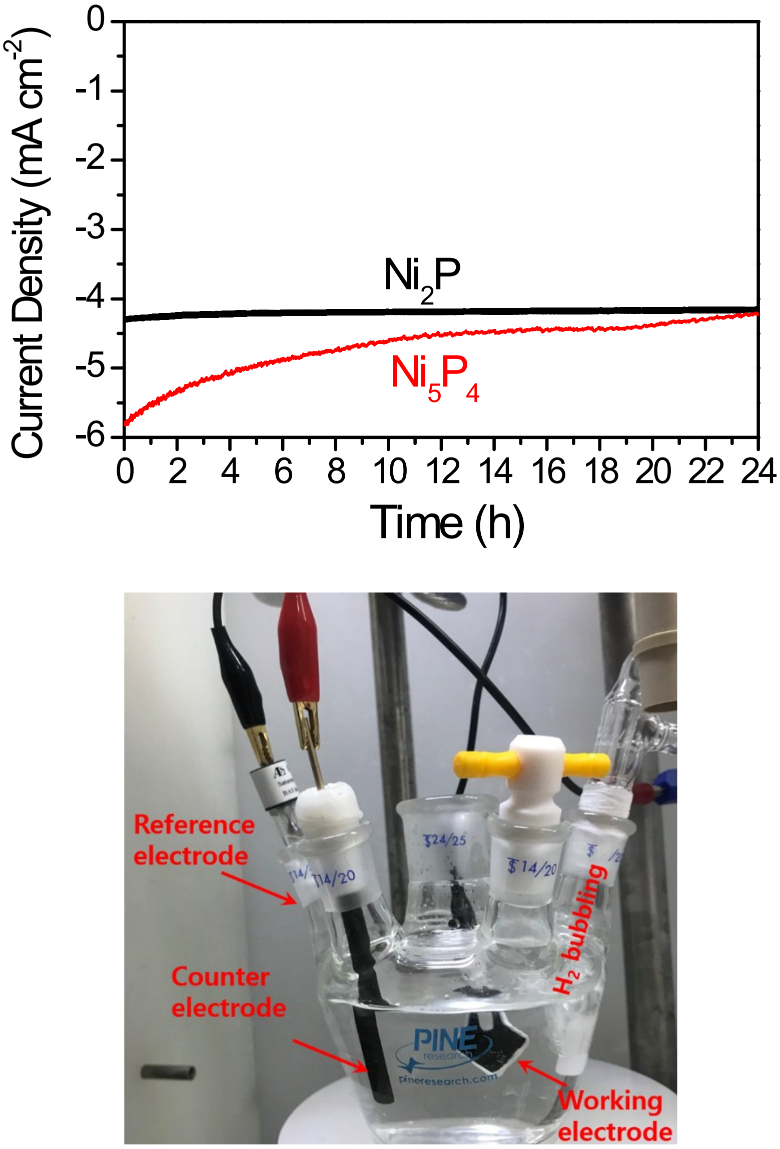

Fig. S7 Chronoamperometric responses at 0.10 V, showing a current attenuation of 0.5% and 27% for Ni_2P and Ni_5P_4, respectively, in 0.5 M H_2SO_4 after 24 h. Photograph shows the cell setup when the graphite rod was used as counter electrode. The counter electrode was shielded by a membrane that blocks the transmission of dissolved C ions or carbon particles into the electrolyte.

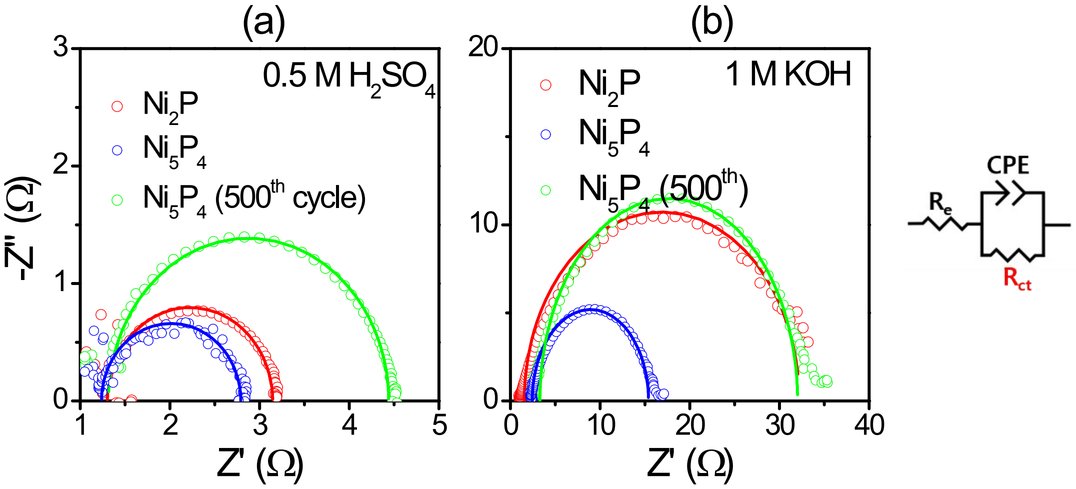

Fig. S8 Nyquist plots for electrochemical impedance spectroscopy (EIS) for Ni_2P and Ni_5P_4 in the frequency range of 100 kHz–0.1 Hz and an amplitude of 10 mV at $\eta = 0.15$ V, before and after 24 h (500 cycles) in (a) 0.5 M H_2SO_4 (pH 0) and (b) 1 M KOH (pH 14) electrolytes. An equivalent circuit model is shown in the right.

In the high-frequency limit under non-Faradaic conditions, the electrochemical system is approximated by the modified Randles circuit shown in the right, where R_s denotes the solution resistance, CPE is a constant-phase element related to the double-layer capacitance, and R_{ct} is the charge-transfer resistance from any residual Faradaic processes. A semicircle in the low-frequency region of the Nyquist plots represents the charge transfer process, with the diameter of the semicircle reflecting the charge-transfer resistance. The real and negative imaginary components of the impedance (Z' and $-Z''$) are used as the x and y axes, respectively. Simulating the EIS spectra using an equivalent circuit model allowed us to determine R_{ct}, which is a key parameter for characterizing the catalyst-electrolyte charge transfer process.

The R_{ct} values at pH 0 are 2 and 1.5 Ω, for Ni_2P and Ni_5P_4, respectively, before the cycle. The R_{ct} of Ni_5P_4 become 3.3 Ω, after the 500^{th} cycle. The value of R_{ct} is consistent with their HER performance. The value of R_{s} is 1.2 Ω. The R_{ct} is 30 and 12 Ω, for Ni_2P and Ni_5P_4, respectively, before cycle at pH 14. The R_{ct} of Ni_5P_4 increases to 30 Ω after the 500^{th} cycle. The value of R_{s} is 2 Ω. We conclude that the charge-transfer resistance plays a major role in determining the catalytic activity.

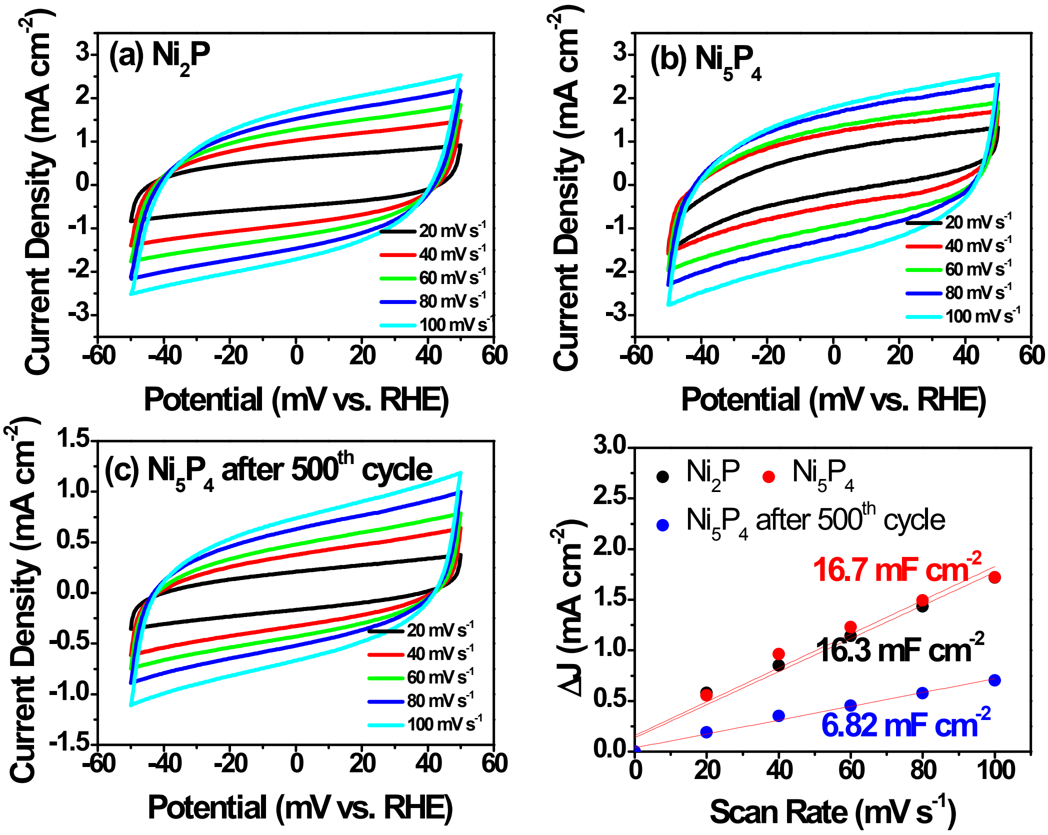

Fig. S9 Cyclovoltammetry curves of (a) Ni_2P, (b) Ni_5P_4, and (c) Ni_5P_4 after 500th cycle in a non-Faradaic region (-50 mV ~ 50 mV), at 20–100 mV s^{-1} scan rates and in 0.5 M H_2SO_4 solution. (d) Difference (ΔJ) between the cathodic discharging and anodic charging currents measured at 0 V (vs. RHE) plotted as a function of the scan rate (20, 40, 60, 80, and 100 mV s^{-1}).

Cyclovoltammetry curves were measured at -0.05 ~ 0.05 V, in a non-Faradaic region, using various scan rates. The double-layer capacitance (C_{dl}) was obtained as the slope of a linear fit of ΔJ vs. scan rate, where ΔJ represents the average value of the cathodic discharging and anodic charging currents. The C_{dl} values of Ni_2P and Ni_5P_4 are 16.3 and 16.7 mF cm^{-2}, respectively, showing a similar value. After 500th cycle, the C_{dl} of Ni_5P_4 decreased to 6.82 mF cm^{-2}. Electrochemical active surface area (ECSA) was estimated from the C_{dl} using the equation: ECSA = $C_{\mathrm{dl}}/C_{\mathrm{s}}$, where C_s = 0.035 mF cm^{-2}.[S1] The ECSA is 466 and 477 mF cm^{-2} for Ni_2P and Ni_5P_4, respectively.

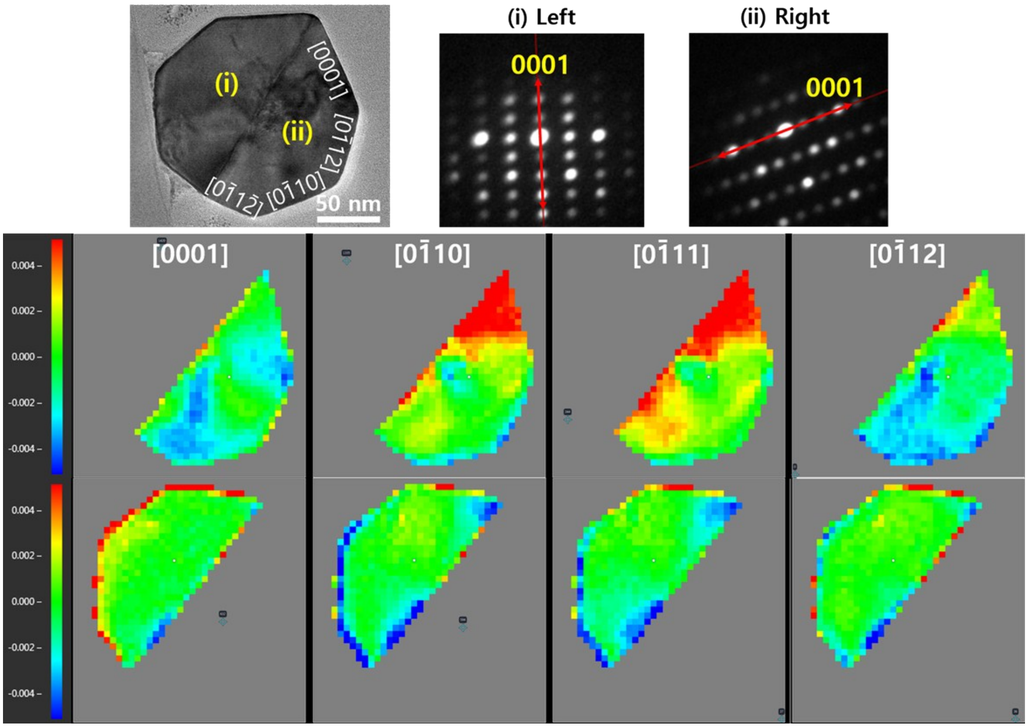

Fig. S10 HRTEM images for the octagonally shaped cross section of Ni_2P NW before the cycle; NBED pattern (zone axis = [0110]) for the (i) left and (ii) right twin segments and corresponding strain maps along the [0001], [012], [010], and [01] directions. The [0001] directions are marked in NBED patterns. Strain maps of the lattice contraction (negative value, blue) or expansion (positive value, red) relative to a reference at the center of NW (marked by the white dots), where no lattice deformation presumably occurs, were taken on the given direction. The strain mappings indicate that the range of the strain is within ±0.5%. There is negligible strain at any direction.

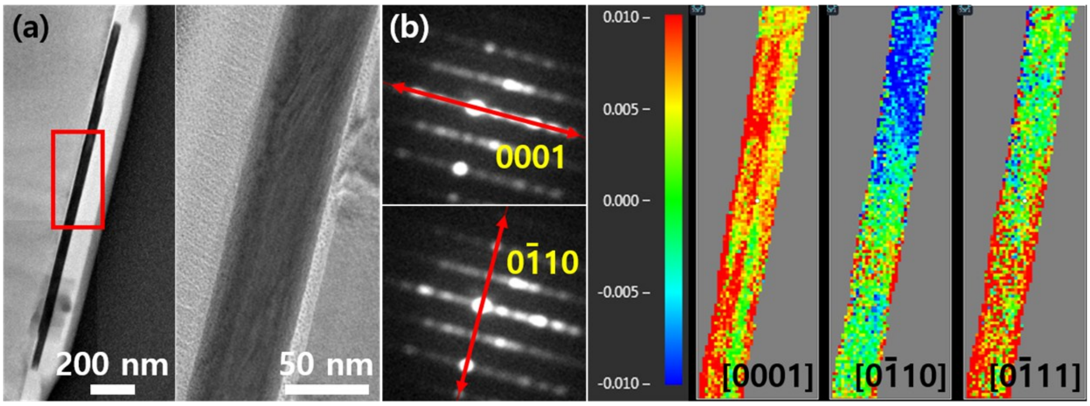

Fig. S11 (a) HRTEM images for the lateral planes of Ni_5P_4 NS before the cycle. (b) NBED patterns (zone axis = [010]), and its corresponding strain maps along the [0001], [010], and [011] directions. The first two directions are marked in NBED patterns. The scale bars indicate the range of the strain (±1%). Strain maps of the lattice contraction (negative value, blue) or expansion (positive value, red) relative to a reference at the center of NW (marked by the white dots), where no lattice deformation presumably occurs, were taken on the given direction. The strains appear randomly because the stacking faults in the nanowires. But there is no specific strain at the surface.

(a)

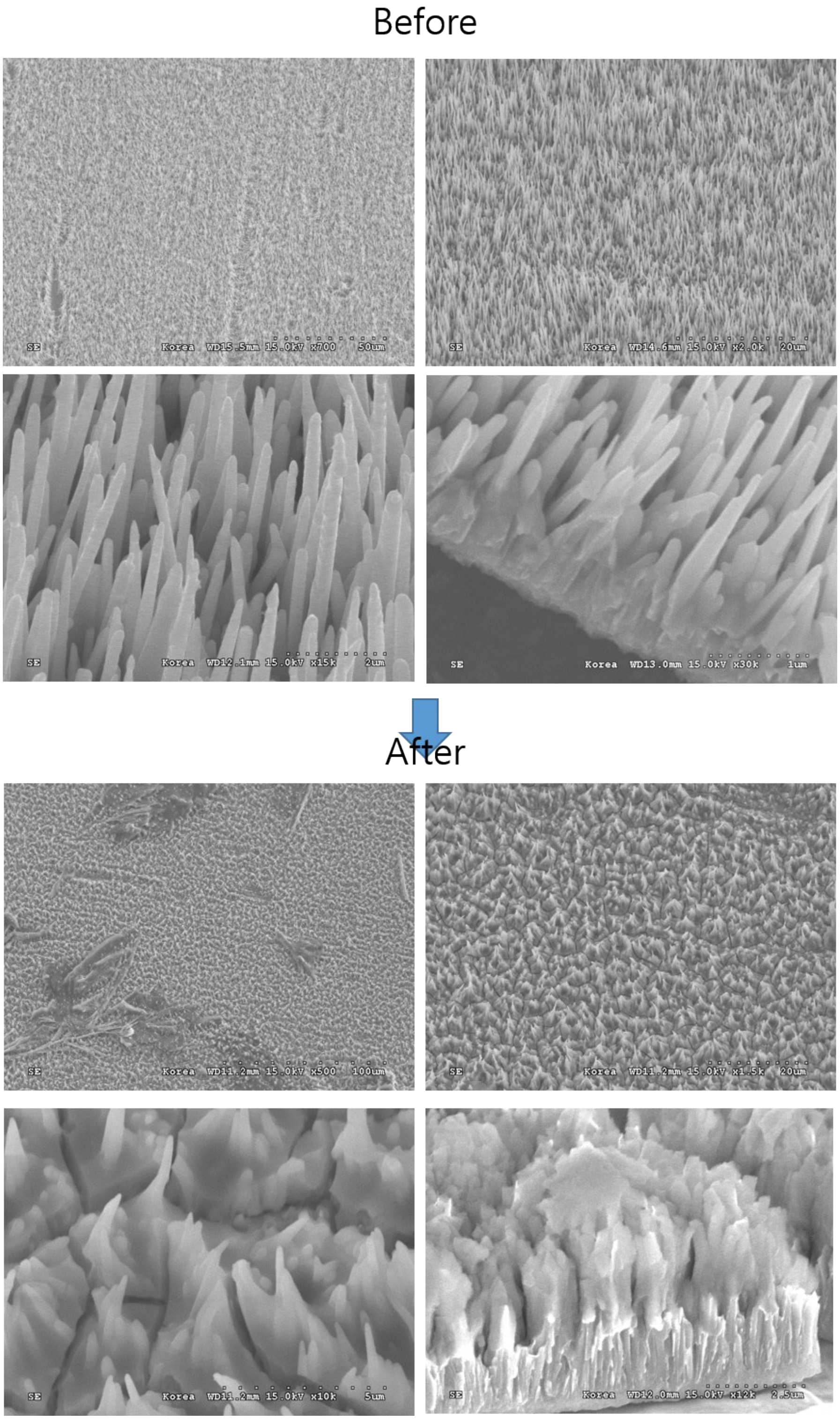
Before
SE Korea WD15.5mm 15.0kV x700 50um
SE Korea WD14.6mm 15.0kV x2.0k 20um
SE Korea WD12.1mm 15.0kV x15k 2um
SE Korea WD13.0mm 15.0kV x30k 1um
After
SE Korea WD11.2mm 15.0kV x500 100um
SE Korea WD11.2mm 15.0kV x1.5k 20um
SE Korea WD11.2mm 15.0kV x10k 5um
SE Korea WD12.0mm 15.0kV x12k 2.5um

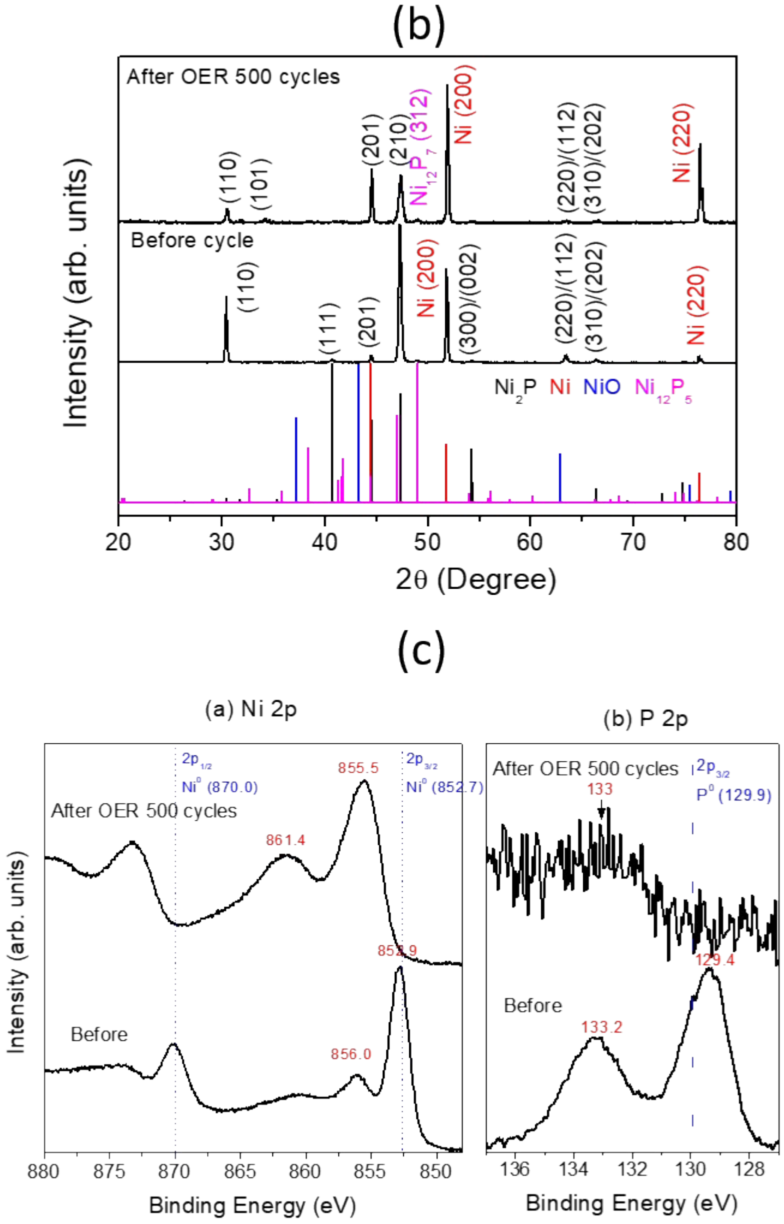

Fig. S12 (a) SEM images, (b) XRD pattern, and (c) XPS of Ni_2P NW array before and after 500 cycled OER LSV scan in 1 M KOH.

The SEM images reveal that after the 500 cycles, the Ni_2P NWs are covered by amorphous oxide layers, and the films underneath the Ni_2P NW array are cracked. EDX data confirms the oxide layers onto the Ni_2P NWs (not shown here).

The XRD peaks of the Ni_2P NW sample after the 500 cycles are indexed using those of references: cubic phase Ni (JCPDS No. Fm**Error!**m, 87-0712, $a = 3.523$ Å), hexagonal phase Ni_2P (JCPDS No. 74-1385, P2m, $a = 5.859$ Å, $c = 3.382$ Å), cubic phase NiO (JCPDS No. 78-0643, Fm**Error!**m, $a = 4.176$ Å), and $Ni_{12}P_5$ (JCPDS No. 74-1381, I4/m, $a = 8.646$ Å, $c = 5.076$ Å). For comparison, the XRD pattern of the sample before the cycle is displayed. After 500 cycles, the relative intensity of the Ni_2P peaks to that of the Ni peak decreased. A small peak of $Ni_{12}P_5$ is identified. But no NiO peaks are detected,

For as-grown Ni_2P NWs (before cycle), the $2p_{3/2}$ peak consisted of three bands at 852.9 (0.2) and 856.0 (3.3), which were assigned to Ni(I)-P and Ni(III)-P/Ni(III)-O, respectively. The value in parenthesis represents the blue shift from the peak position of neutral Ni^0 (852.7 eV). After 500 cycles, the Ni $2p_{3/2}$ peak consisted of two bands at 855.5 (2.8) and 861.4 (8.5) eV. These peaks are assigned to the Ni(III)-O bond and the shake-up satellite peak, respectively. The stronger satellite peak is due to the increased population of Ni(III)-O bonds.

Before the cycle, the Ni_2P NWs show P 2*p* bands at 129.4 and 133.2 eV, which are ascribed to the P-Ni and P-O bonding structures, respectively. After 500 cycles, the P-Ni band is significantly reduced, and the P-O band becomes the primary band.

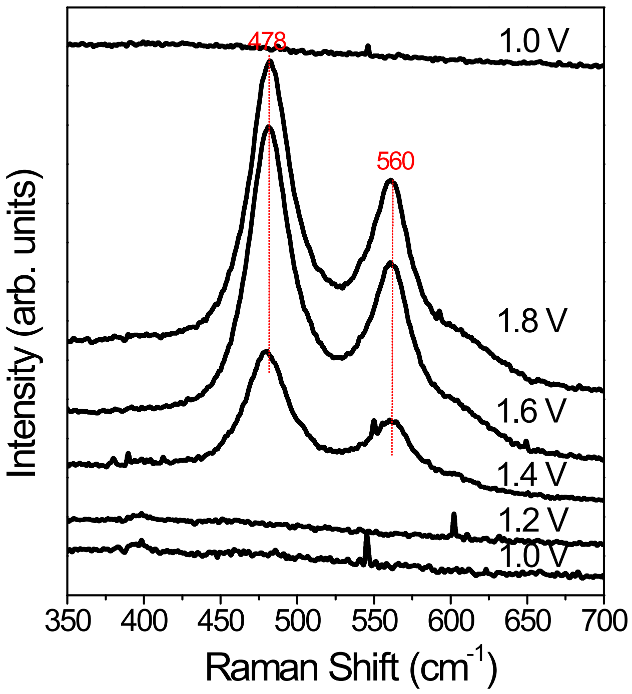

Fig. S13 *In situ* Raman spectra of Ni_2P NWs in 0.1 KOH as the potential (vs. RHE) increases from 1.0 to 1.8 V and returns to 1.0 V. Excitation wavelength is 514.5 nm (Ar ion laser). Each spectrum (displayed as an upward stacked temporal sequence) was acquired over 10 s starting at the electrode potentials as indicated. As the potential is raised toward 1.3 V (the potential at which OER occurs), two peaks appear at 478 and 560 cm^{-1}. These are assigned to the Ni-O vibrational mode of the Ni-OOH.[S26-S28] As the potential decreases to 1.0 V, the peaks disappear. We confirmed the production of Ni-OOH intermediates during OER.

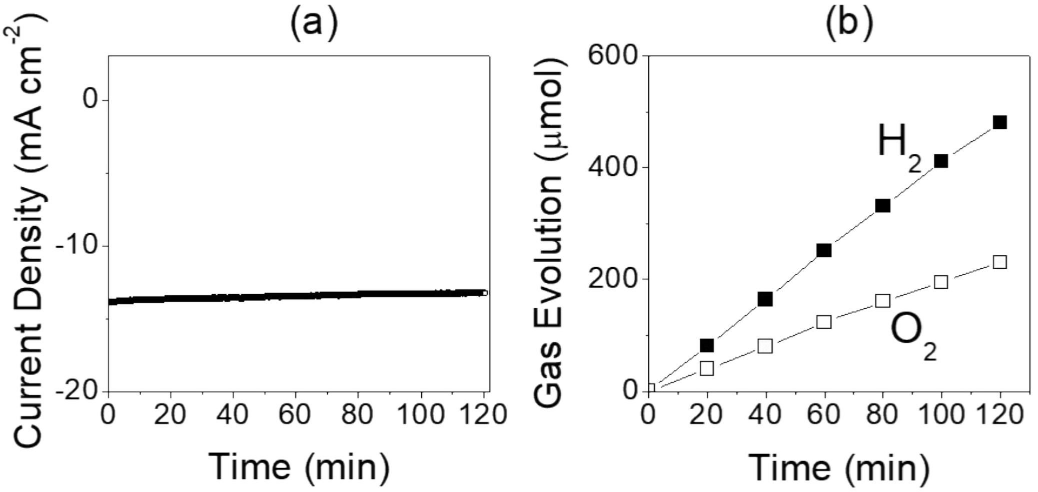

Fig. 14. (a) Stability of current and (b) H_2 and O_2 evolution vs. time (min) for Ni_2P NWs under an applied potential of -0.1 V (vs. RHE) in pH 13.

The current showed excellent stability over 120 min (2 h). The gas chromatography data was summarized in **Table S3** (see below). Faradic efficiency (*FE*) for the production of H_2 and O_2 was calculated by the equations: $FE_{H2} = \frac{2 \times N_{H_2} \times 96485}{Q}$ and $FE_{O2} = \frac{4 \times N_{O_2} \times 96485}{Q}$, where N_{H2} and N_{O2} are the amount (mol) of H_2 and O_2, respectively, and Q is the total amount of generated charge in coulomb (= current × time). The Faradaic efficiency for H_2 generation, O_2 generation, and water splitting was 98%, 95%, and *ca.*97%, respectively. The molar ratio of $[H_2]/[O_2]$ is avg. 2.06. The slight excess of H_2 is probably due to the slow kinetics of O_2 evolution at the anode.

Table S3. Amount (μmol) of evolved H_2 and O_2 as a function of time for a duration of 120 min (2 h) and Faradaic efficiency (FE) for the production of H_2 and O_2.

Time (min)	Current density (mAcm^{-2})	Gas Evolution (μmol)			Faradic Efficiency (%)	
		H_2	O_2	$[H_2]/[O_2]$	H_2	O_2
20	13.9	81.3	39.8	2.04	94	92
40	13.5	163.8	79.8	2.05	98	95
60	13.5	252.1	123.4	2.04	100	98
80	13.5	332.1	161.2	2.06	99	96
100	13.5	410.9	195.2	2.10	98	93

120	13.3	480.9	230.8	2.08	97	93
Average				2.06	98	95

IV. References

S1. C. C. L. McCrory, S. Jung, J. C. Peters and T. F. Jaramillo, *J. Am. Chem. Soc.*, 2013, **135**, 16977−16987; C. C. L. McCrory, S. Jung, I. M. Ferrer, S. M. Chatman, J. C. Peters and T. F. Jaramillo, *J. Am. Chem. Soc.*, 2015, **137**, 4347-4357.

S2. J. Kibsgaard, C. Tsai, K. Chan, J. D. Benck, J. K. Nørskov, F. Abild-Pedersen and T. F. Jaramillo, *Energy Environ. Sci.,* 2015, **8**, 3022--3029

S3. A. B. Laursen, R. B. Wexler, M. J. Whitaker, E.J. Izett, K. U. D. Calvinho, S. Hwang, R. Rucker, H. Wang, J. Li, E. Garfunkel, M. Greenblatt, A. M. Rappe and G. Charles Dismukes, *ACS Catal.* 2018, **8**, 4408-4419.

S4. Y. Shi, Y. Xu, S. Zhuo, J. Zhang and B. Zhang, *ACS Appl. Mater. Interfaces,* 2015, **7**, 2376-2384.

S5. X. Wang, Y. V. Kolenko and L. Liu, *Chem. Commun.*, 2015, **51***,* 6738-6741.

S6. X. Wang, Y. V. Kolenko, X. Q. Bao, K. Kovnir and L. Liu, *Angew. Chem. Int. Ed.*, 2015, **54**, 8188-8192.

S7. M. Ledendecker, S. K. Calderón, C. Papp, H. P. Steinrück, M. Antonietti and M. Shalom, *Angew. Chem. Int. Ed.*, 2015, **54**, 12361-12365.

S8. L. A. Stern, L. Feng, F. Song and X. Hu, *Energy Environ. Sci.*, 2015, **8**, 2347-2351.

S9. A. Han, H. Chen, Z. Sun, J. Xu and P. Du, *Chem. Commun.*, 2015, **51**, 11626-11629.

S10. B. You, N. Jiang, M. Sheng, W. Bhushan and Y. Sun, *ACS Catal.*, 2016, **6**, 714-721.

S11. G. F. Chen, T. Y. Ma, Z. Q. Liu, N. Li, Su, Z. Y. K. Dave and S. Z. Qiao, *Adv. Funct. Mater.*, 2016, **26**, 3314-3423.

S12. J. Li, J. Li, X. Zhou, Z. Xia, W. Gao, Y. Ma and Y. Qu, *ACS Appl. Mater. Interfaces*, 2016**,** **8**, 10826-10834.

S13. X. Y. Yu, Y. Feng, B. Guan, X. W. Lou and U. Paik, *Energy Environ. Sci.*, 2016, **9**, 1246-1250.

S14. X. Wang, W. Li, D. Xiong and L. Liu, *J. Mater. Chem. A*, 2016, **4**, 5639-5646.

S15. P. W. Menezes, A. Indra, C. Das, C. Walter, C. Göbel, V. Gutkin, D. Schmeiβer and M. Driess, *ACS Catal.*, 2017, **7**, 103-109.

S16. Y. Li, H. Zhang, M. Jiang, Q. Zhang, P. He and X. Sun, *Adv. Funct. Mater.*, 2017, **27**, 1702513.

S17. J. Xu, Wei, K. X. J. D. Costa, J. L. Lado, B. Owens-Baird, L. P. L. Gonçalves, S. P. S. Fernandes, M. Heggen, D. Y. Petrovykh, R. E. Dunin-Borkowski, K. Kovnir and Y. V. Kolen'ko, *ACS Catal*., 2017, **7**, 5450-5455.

S18. Z. Yin, C. Zhu, C. Li, S. Zhang, X. Zhangc and Y. Chen, *Nanoscale*, 2016, **8**, 19129-19138.

S19. S. L. M. Schroeder, G. D. Moggridge, R. M. Ormerod, T. Rayment and R. Lambert, *Surf. Sci.*, 1995, **324**, L371-L377.

S20. B. H. Frazer, B. Gilbert, B. R. Sonderegger and G. De Stasio, *Surf. Sci.*, 2003, **537**, 161-167.

S21. B. K. Teo, *EXAFS: Basic Principles and Data Analysis* (Springer-Verlag, Berlin, 1986, pp 92).

S22. M. P. Scah and M. A. Dench, *Interface. Anal*., 1, 2, 1979.

S23. Z. Huang, Z. Chen, Z. Chen, C. Lv, H. Meng and C. Zhang, *ACS Nano*, 2014*,* **8**, 8121-8129.

S24. Z. Pu, Q. Liu, A. M. Asiri and X. Sun, *Nanoscale*, 2014, **6**, 11031–11034.

S25. Y. Shi, Y. Xu, S. Zhuo, J. Zhang and B. Zhang, *ACS Appl. Mater. Interfaces*, 2015, **7**, 2376−2384.

S26. B. S. Yeo and A. T. Bell, *J. Phys. Chem. C*, 2012, **116**, 8394-8400.

S27. M. W. Louie and A. T. Bell, *J. Am. Chem. Soc.*, 2013, **135**, 12329-12337.

S28. I. H. Kwak, H. S. Im, D. M. Jang, Y. W. Kim, K. Park, Y. R. Lim, E. H. Cha and J. Park, *ACS Appl. Mater. Interfaces*, 2016, **8**, 5327-5334.